Comment on: "Investigating Earth's Formation History Through Copper & Sulfur Metal–Silicate Partitioning During Core-Mantle Differentiation" by Mahan et al. (2018)

Eleanor S Jennings[1*], Jon Wade[2], Xavier Llovet[3]

[1]Department of Earth and Planetary Sciences, Birkbeck, University of London, Malet Street, London, WC1E 7HX, United Kingdom *corresponding author: e.jennings@bbk.ac.uk

[2]Department of Earth Sciences, University of Oxford, South Parks Road, Oxford, OX1 3AN, United Kingdom

[3]Scientific and Technological Centres, Universitat de Barcelona, Lluís Solé i Sabarís, 1-3, 08028 Barcelona, Spain

Key points:

- EPMA analyses of small areas are prone to analytical artifacts such as fluorescence that can be problematic when measuring minor elements
- In the study of Mahan et al. (2018), fluoresced Cu X-rays from the Cu sample holder account for ~70% of their measured Cu concentrations
- We quantified the contribution of spurious Cu X-rays to the primary signal using Monte Carlo particle transport simulations

Abstract

The physical and chemical conditions of terrestrial core formation play a key role in the distribution of elements between the Earth's silicate mantle and metallic core. To explore this, Mahan et al. (2018a) present experimentally-derived partitioning data, showing how Cu distributes itself between metal and silicate at lower-mantle PT conditions with implications for planetary accretion and core formation. Eight experiments were performed in a diamond anvil cell (DAC) and each sample was welded to a copper grid for analysis. An offset in partitioning behaviour was subsequently noted between the high-P experiments and the lower-P dataset. However, when analysing the DAC experiments by electron probe microanalysis, the authors did not account for the secondary fluorescence of Cu that arises from the sample holder. Using Monte Carlo simulations of X-ray and electron transport, we show that the fluorescence of the Cu grid, originating from high energy continuum X-rays emitted from the sample, makes a significant contribution to the reported measurement of Cu in both the silicate and metallic phases. This is in good agreement with previous measurements made on Cu-free analogues. On average, around 70% of the published Cu concentrations are attributable to X-rays that originate externally to the sample. The reported offset in $K_D^{met-sil}$ at high pressures may reflect the different experimental and analytical protocol used, rather than a true pressure effect. Although adequate *post-hoc* corrections can be made, uncertainties around the exact sample and detector geometries make it difficult to refine simulations and derive accurate correction factors for each experiment.

1   Introduction

Core formation occurs sequentially during planetary accretion when immiscible and dense molten metallic material sinks through liquid and solid silicates (e.g. Rubie et al., 2011). By understanding how various elements distribute themselves between metal and silicate as a function of T, P, and composition, inferences can be made concerning the conditions planetary formation and core segregation (e.g. Jones and Drake, 1986; Walter et al., 2000; Wood et al., 2006).

In order to understand the high-PT partitioning behaviour of various elements of interest, scientists have traditionally performed experiments at elevated P (≥1 GPa) and T (≥1500 K) conditions using large-volume presses: the piston cylinder and multi-anvil. Run products are

straightforwardly analysed by electron probe microanalyser (EPMA) (e.g. Jones and Drake, 1986; Righter et al., 1997; Wade and Wood, 2005; Siebert et al., 2011). More recently, there has been a focus on extending these partitioning relationships to higher-PT conditions that are relevant to deep planetary interiors. This was initially achieved by Bouhifd and Jephcoat (2003), who examined Ni partitioning using a laser-heated diamond anvil cell (DAC). DAC partitioning experiments have now been widely adopted and extended to a broad range of siderophile and light element partitioning investigations (Frost et al., 2010; Bouhifd and Jephcoat, 2011; Siebert et al., 2012, 2013, 2018; Fischer et al., 2015; Badro et al., 2016; Blanchard et al., 2017; Chidester et al., 2017; Suer et al., 2017; Mahan et al., 2018a,b). The increase in enthusiasm for such experiments may be related to the dramatic improvements in sample recovery and preparation afforded by dual-beam focused ion beam (FIB) instruments. Of key importance is the small size of the DAC run products, with samples routinely prepared as ~1 – 4 µm thick lamella just 10s of µm long; for ease of handling these are typically welded to copper transmission electron microscopy (TEM) "lift-out" grids (e.g. Omniprobe or PELCO). Such grids are usually flat, hemi-spherical and around 1 x 3 mm and 25 – 35 µm thick, and have several prongs of around 100 µm width onto which lamellae can be FIB-welded using Pt deposition.

In the study of Mahan et al. (2018a), where the high-pressure partitioning behaviour of Cu between adjacent metal and silicate phases is explored, the presence of this Cu grid may be problematic. This study utilised both FIB-prepared high-pressure DAC experiments and lower pressure, larger volume, experiments. The latter experiments were prepared in the 'traditional' way, mounted and polished in epoxy and, importantly, without a Cu grid. The authors noted that high-pressure experiments are offset to lower $K_{Cu}^{met-sil}$ values than expected from the low-pressure trend, i.e. that Cu partitions more strongly into silicate. This was interpreted to imply that, with increasing equilibration pressure, Cu becomes increasingly less siderophile than previously thought. However, we demonstrate that the DAC analyses published by Mahan et al. (2018a) are severely compromised by secondary X-ray fluorescence of the Cu holder. For five experiments, corrections for secondary fluorescence bring the measured concentrations to within error of zero. For the remaining three, corrections slightly raise the calculated K, bringing high-pressure data a little closer to the low-pressure trend.

1.1   Secondary fluorescence in EPMA measurements

EPMA is ideally suited for the quantified elemental analysis of DAC partitioning experiments: it is convenient to use, quantification methods are mature, and the small spatial scales preclude the use of most other methods. The size of the run products, and the features of interest that they contain, necessitates that the analytical areas available for measurement are chemically homogenous on the scale of a few μm^2. For DAC experimental analysis, EPMA is being used close to its spatial resolution limits, and particular consideration must be given to analytical artefacts such as fluorescence arising from neighbouring phases (Reed and Long, 1963; Wade and Wood, 2012). Although the concept of the electron interaction volume is familiar to most EPMA users, generation of secondary X-rays resulting from fluorescence at a distance from the analytical spot is rarely considered. Here, secondary fluorescence occurs when a characteristic X-ray is generated by absorption of an X-ray of energy higher than that of the absorption edge (either a continuum or characteristic X-ray). The mean free path of an X-ray is dependent on both the media through which it passes and its energy: travelling through a basaltic glass, a bremsstrahlung X-ray with an energy of e.g. 12 keV can travel a distance of ~220 μm. For elemental partitioning or diffusion studies, where minor element concentrations are necessarily measured near phases containing that element at high concentrations, this can be particularly problematic (e.g. Fournelle et al., 2005; Wade and Wood, 2012; Borisova et al., 2018).

Typically, secondary fluorescence presents only a minor contribution to an analysis, since spatial distances to phase boundaries are large and thus X-rays are effectively attenuated within the phase of interest. In DAC experiments, such as presented by Mahan et al (2018a), a key assumption required for high quality minor element analysis by EPMA is violated; namely, the material is not homogeneous on the scale of the X-ray fluoresced volume. For the trace element analysis of Cu detailed here, these effects are exacerbated by the sample preparation which uses a Cu TEM grid, welded to the sample and visible in the micrographs. Using a 15 kV, 15 nA focused beam, Jennings et al. (2019) measured up to >1 wt.% of Cu in thin lamellae of Cu-free samples (CFMAS basalt and Fe-alloy) that were welded to Cu TEM grids in a similar geometry to that used

by Mahan et al. (2018a) (Figure 1). This spurious signal arose solely from secondary fluorescence of the Cu holder. Increased accelerating voltages with a larger continuum tail above the Cu K absorption edge will further exacerbate the erroneous Cu concentration.

Mahan et al. (2018a) investigated Cu partitioning with a similar analytical setup to that used for Figure 1, where samples were welded to Cu TEM grids (e.g. Siebert et al., 2018) and subsequently analysed at 20 kV and 20 nA with a 1 µm spot. Taken in isolation, the presented Cu partitioning data show no clear change with temperature, despite the reported high temperature-dependence (Mahan et al., 2018a): this provides an initial indication that the dataset is analytically compromised (Figure 2). The authors do appear aware of possible analytical artefacts and caveat their data by measuring Cu concentrations in both phases using quantified EDS and WDS detectors. They suggest that both are "indistinguishable within error, indicating a lack of analytical artefacts (e.g. TEM grid contamination)" (Mahan et al., 2018a). This is, however, a misdirection - both types of detector measure the same phenomenon, and it would be surprising if they did not yield a similar apparent concentration. A small difference in measured secondary fluorescence may be expected because a lower (15 kV) accelerating voltage beam was employed for the EDS measurements. However, this is somewhat counteracted by the larger solid angle of the EDS detector and the resultant decrease in spectrometer defocusing (Buse et al., 2018). The EDS detector is also located in a different position inside the instrument. This level of detail is likely lost in the lower precision afforded by EDS analysis.

Below, we quantify the secondary fluorescence contribution to the measurements presented in Mahan et al. (2018a) to asses any implications for the validity of fitted parameterisations of Cu partitioning.

2   Method

We modelled the fluorescence contribution of the Cu sample holder with realistic geometries derived from the work of Mahan et al. (2018a). Monte Carlo simulations were performed with the simulation package PENEPMA (v.2014; Llovet and Salvat, 2017). This package is optimised for EPMA applications and is based on the general-purpose code PENELOPE (Salvat, 2015). PENEPMA simulates realistic sample and detector geometries and beam conditions. We applied

interaction forcings to increase computational efficiency (Llovet and Salvat, 2018). The accuracy of secondary fluorescence simulations has been demonstrated in many previous studies (e.g. Llovet et al, 2012, and references therein; Borisova et al., 2018).

Although simulations were performed using a realistic sample geometry for the measurements of Mahan et al. (2018a), they inevitably involve assumptions and simplifications. Additional images of the experiments of Mahan et al. (2018a) are given by Siebert et al. (2018) and Mahan et al. (2018b). These indicate that the experimental sample lamella is usually welded to the left-hand side of a Cu post, with the weld being on the short edge. They also show variations in the sample dimensions and homogeneity that we cannot easily account for, but do indicate that the general configuration and shape of the metal and silicate phase (always a near-symmetrical sphere surrounded by an oblate sphere of silicate) are constant, allowing simulations to be performed for a generalised sample geometry. Guided by these published works and prior experience, we have chosen to simulate the following geometry:

a) Sample lamella are 20 x 12 x 3 µm, connected to the Cu holder along the short edge. The sample consists of a central pure iron sphere (6 µm diameter, positioned in the centre of the lamella, truncated at top and base).The remaining volume was filled with a CFMAS basaltic glass composition (13.0 wt.% MgO, 22.4 wt.% Al_2O_3, 46.4 wt.% SiO_2, 11.2 wt.% CaO, 5.1 wt.% Fe_2O_3). In all cases, the simulated silicate and metals are Cu-free.

b) The Cu block representing the holder is 100 x 100 x 25 µm, as manufacturer specifications of the thickness range from 25 – 35 µm. The flat top surface of the Cu is flush with that of the lamella. Lamella and Cu block are lying flat, i.e. the shortest dimension is the beam-parallel z-axis.

c) Pt welds are not included as they are spatially variable and volumetrically minor – they may however be apparent in the actually analyses.

The geometry file and an illustration of the geometry are provided as supplemental files. An annular (360°) detector was simulated for increased computational efficiency, with a latitudinal angular opening of 10° centred on a 40° take-off angle, as is usual for WDS detectors (setup illustrated in Wade and Wood, 2012). A focused electron beam of 20 kV accelerating voltage was used and simulations ran until a relative uncertainty of 2% (at 3σ level) was achieved on Cu $K\alpha_1$.

X-rays were also counted using smaller detectors with a 10° azimuthal width placed at 90° intervals, which better reflect the solid angle of a commercial EPMA spectrometer when the flux of outgoing X-rays has no axial symmetry about the z-axis. For these detectors, simulations ran until a relative uncertainty of 5% (at 3σ level) was achieved on Cu Kα$_1$.

In order to compare simulated counts with the reported matrix-corrected concentrations of Mahan et al. (2018a), we simulated measurements of thick 1mm diameter cylindrical standards of pure Cu, CFMAS glass, and pure Fe. A ZAF correction was performed with the ZAF$_{sample}$/ZAF$_{std}$ ratio determined using CalcZAF (after CITZAF; Armstrong, 1995).

An initial simulation was performed with the beam centred on the metallic and silicate portion of the sample, with a low energy cut-off at 1 keV (energy at which electrons are considered to be absorbed in the sample). A transect across the sample, perpendicular to the Cu interface, was subsequently performed with a 6 keV low-energy cut-off to reduce computation time, with the same ZAF$_{sample}$/ZAF$_{std}$ used to convert Cu counts to concentrations (note that electrons with energy below 8.98 keV can no longer generate Cu Kα X-rays).

3   Results

The apparent Cu concentrations "measured" in the sample at various distances from the Cu sample holder are shown in Figure 3a. Secondary fluorescence is significant throughout the sample, with the apparent Cu concentration decreasing approximately exponentially with distance within a given material. Secondary fluorescence of Cu is more severe when the iron is analysed relative to the basaltic glass, explained by an increase in the intensity of higher-energy continuum radiation: in comparison to the silicate, the higher Z iron results in increased production of bremsstrahlung X-rays with energies exceeding that of the Cu K absorption edge. The variations in spatial distribution of apparent Cu concentration may be obscured by analytical noise in real measurements. Secondary fluorescence is aided by the fact that the basalt does not strongly attenuate X-rays, and that X-rays can also pass efficiently through the empty space (vacuum) underneath and beside the thin lamella, impacting the side of the Cu holder.

The detector position relative to the sample has a minor effect upon the measured fluorescence across an interface, since absorption of the fluoresced X-rays depends on the

material through which they travel to the spectrometer (e.g. Fournelle et al., 2005; Buse et al., 2018). Figure 3b shows that the maximum fluorescence is, perhaps counterintuitively, measured away from the Cu sample holder. This can be explained by the small dimensions of the DAC sample, which attenuates fewer Cu X-rays than the much larger Cu block itself. This directional bias is impossible to estimate for published data, since knowledge is required of a) sample orientation, and b) measuring spectrometer location. A hypothetical annular detector allows an average X-ray intensity to be acquired, independent of actual spectrometer orientation, which may introduce a systematic error of up to ~ 20%. We use a simulated annular detector to approximate the analytical measurements, but caution that these may only give the approximate magnitude of the fluoresced contributions.

PENEPMA also tracks the origin of secondary X-rays, showing that they are generated through the full depth of the Cu grid, and from up to ~ 10 μm within it (Figures 4 and 5).

4   Discussion

Assuming that measurements of the metallic phase were made in the central two thirds of the sphere (Siebert et al., 2018), the minimum measured Cu concentration, arising purely from fluorescence of the Cu holder, is ~1 wt.% (Figure 3a). Silicate measurements are usually reported as being the average of a few analyses (N = 2 to 4, Mahan et al., 2018a), and although it is not possible to deduce their precise location with respect to the Cu holder, the samples shown in Siebert et al. (2018) and Mahan et al. (2018ab) (figures 2, 1 and 1 respectively) reveal only limited space for analysis. Assuming an even number of measurements are made at +/-6 μm either side of the metal sphere centre (so +/- 3.6 μm from the interface), we find a mean apparent CuO concentration of 0.8 wt.%.

Given the aforementioned assumptions and the inherent variations of the samples, these apparent concentrations may not be accurate for every experiment. However, the magnitude indicates the approximate contribution of secondary fluorescence to the reported data, and we would suggest that these contributions are correct to within around 25 % for all DAC experiments reported here.

Whilst bearing these caveats in mind, we can use these simulated fluorescence contributions to correct the measurements presented in Mahan et al. (2018a). This secondary fluorescence contribution can be considered as a linear addition to the primary X-ray yield arising from the experimental materials. As such, the concentration data can simply be corrected for fluorescence (note that one should actually deal with X-ray intensity ratios rather than concentrations, but raw data are rarely reported). We find that some measured concentrations are now at or below 0 wt.%: by taking these as 0 wt.%, we find the mean Cu concentration measured in metal has decreased from 2.3 to 1.0 wt.%, and the mean CuO in silicate has decreased from 1.3 to 0.5 wt.%. On average, fluorescence accounts for 68 % and 72 % of the signal for metal and silicate, respectively.

If we use the same absolute measurement uncertainties after the linear correction, then five out of the eight experiments have a silicate and/or metal Cu concentration that is either below zero, or within uncertainty of it. We have recalculated $\log K_{\mathrm{Cu}}^{\mathrm{met\text{-}sil}}$ from the remaining three experiments (Figure 6) by calculating approximate mole fractions from the data provided and the metal activity coefficients in the Fe-S-Cu ternary system, as detailed by Mahan et al. (2018a). The corrections result in a slightly higher $\log K_{\mathrm{Cu}}^{\mathrm{met\text{-}sil}}$, making Cu a little more siderophile than previously presented. By subtracting a similar Cu concentration from both sides of the ratio, the resulting ratio only changes a little. More to the point, the uncertainty on that ratio is now larger: both concentrations are lower, and the correction factor itself has an unquantified inaccuracy. Fluorescence has introduced a high level of inaccuracy into the published data, and raises the question of whether the conclusions of Mahan et al. (2018a) can be properly supported by just three heavily-corrected data points.

Reduction of the fluoresced signal contribution could be achieved by lowering the electron beam accelerating voltage. Mahan et al. (2018a) performed measurements at 20 keV: using a lower beam energy would result in a drop in intensity of high-energy continuum X-rays, and a consequent reduction in the secondary flourescence contribution. It may also be possible to measure the lower energy Cu L X-ray line, which will be far less susceptible to fluorescence owing to the much lower L-shell fluorescence yield (e.g. Fournelle et al., 2005; Jennings et al., 2019). However, this strategy may introduce other analytical complications (Pouchou, 1996).

5   Conclusions

Secondary fluorescence poses a known difficulty in EPMA measurement when low-concentration measurements are made in the vicinity of high concentrations of a given element. Whilst it is possible to make corrections for fluorescence, inaccuracies are inevitably introduced, particularly when complex geometries are involved. We have demonstrated that the analytical data presented by Mahan et al. (2018a) have been severely compromised by secondary fluorescence from the TEM grid to which they are welded, which is made of copper. This fluorescence has affected silicate and metal measurements similarly, with the published Cu concentrations consisting, on average, of approximately 70 % spurious signal originating externally to the sample. It is difficult to evaluate the exact impact of this on the conclusions of Mahan et al. (2018a), although it would appear that $\log K_{\mathrm{Cu}}^{\mathrm{met\text{-}sil}}$ values would probably increase a little, reducing the offset between low- and high-pressure datasets, and correcting both sides of the ratio would increase the uncertainty of the resultant ratio. The consequences of this potential offset on the presented modelling is uncertain. However, this is a moot point: unavoidable irregularities between real samples relative to simplified simulated X-ray yields means that such a large correction to the measured data is probably unjustified, and thus the DAC data set of Mahan et al. (2018a) must be regarded with caution. We show that it is compromised by systematic analytical errors and so cannot support their stated conclusions.

6   Acknowledgements

7   References

Armstrong, J. T. (1995). CITZAF: a package of correction programs for the quantitative Electron Microbeam X-Ray-Analysis of thick polished materials, thin-films, and particles. *Microbeam Analysis*, *4*(3), 177–200.

Badro, J., Siebert, J., & Nimmo, F. (2016). An early geodynamo driven by exsolution of mantle components from Earth's core. *Nature*, *536*(7616), 326–328. https://doi.org/10.1038/nature18594

Blanchard, I., Siebert, J., Borensztajn, S., & Badro, J. (2017). The solubility of heat-producing elements in Earth's core. *Geochemical Perspectives Letters*, 5, 1–5. https://doi.org/10.7185/geochemlet.1737

Borisova, A. Y., Zagrtdenov, N. R., Toplis, M. J., Donovan, J. J., Llovet, X., Asimow, P. D., et al. (2018). Secondary fluorescence effects in microbeam analysis and their impacts on geospeedometry and geothermometry. *Chemical Geology*, *490*, 22–29. https://doi.org/10.1016/j.chemgeo.2018.05.010

Bouhifd, M. A., & Jephcoat, A. P. (2003). The effect of pressure on partitioning of Ni and Co between silicate and iron-rich metal liquids: a diamond-anvil cell study. *Earth and Planetary Science Letters*, *209*(1–2), 245–255. https://doi.org/10.1016/S0012-821X(03)00076-1

Bouhifd, M. A., & Jephcoat, A. P. (2011). Convergence of Ni and Co metal–silicate partition coefficients in the deep magma-ocean and coupled silicon–oxygen solubility in iron melts at high pressures. *Earth and Planetary Science Letters*, *307*(3–4), 341–348. https://doi.org/10.1016/j.epsl.2011.05.006

Buse, B., Wade, J., Llovet, X., Kearns, S., & Donovan, J. J. (2018). Secondary Fluorescence in WDS: The Role of Spectrometer Positioning. *Microscopy and Microanalysis*, *24*(6), 604–611. https://doi.org/10.1017/S1431927618015416

Chidester, B. A., Rahman, Z., Righter, K., & Campbell, A. J. (2017). Metal–silicate partitioning of U: Implications for the heat budget of the core and evidence for reduced U in the mantle. *Geochimica et Cosmochimica Acta*, *199*, 1–12. https://doi.org/10.1016/j.gca.2016.11.035

Fischer, R. A., Nakajima, Y., Campbell, A. J., Frost, D. J., Harries, D., Langenhorst, F., et al. (2015). High pressure metal–silicate partitioning of Ni, Co, V, Cr, Si, and O. *Geochimica et Cosmochimica Acta*, *167*, 177–194. https://doi.org/10.1016/j.gca.2015.06.026

Fournelle, J. H., Kim, S., & Perepezko, J. H. (2005). Monte Carlo simulation of Nb Kα secondary

    fluorescence in EPMA: comparison of PENELOPE simulations with experimental results. *Surface*

    and Interface Analysis, *37*(11), 1012–1016. https://doi.org/10.1002/sia.2114

Frost, D. J., Asahara, Y., Rubie, D. C., Miyajima, N., Dubrovinsky, L. S., Holzapfel, C., et al. (2010).

    Partitioning of oxygen between the Earth's mantle and core. *Journal of Geophysical Research:*

    Solid Earth, *115*(B2), B02202. https://doi.org/10.1029/2009JB006302

Jennings, E. S., Wade, J., Laurenz, V., & Petitgirard, S. (2019). Diamond Anvil Cell Partitioning

    Experiments for Accretion and Core Formation: Testing the Limitations of Electron Microprobe

    Analysis. *Microscopy and Microanalysis*, *25*(1), 1–10.

    https://doi.org/10.1017/S1431927618015568

Jones, J. H., & Drake, M. J. (1986). Geochemical constraints on core formation in the Earth. *Nature*,

    322(6076), 221. https://doi.org/10.1038/322221a0

Llovet, X., Pinard, P. T., Donovan, J. J., & Salvat, F. (2012). Secondary fluorescence in electron

    probe microanalysis of material couples. *Journal of Physics D: Applied Physics*, *45*(22), 225301.

    https://doi.org/10.1088/0022-3727/45/22/225301

Llovet, X., & Salvat, F. (2017). PENEPMA: A Monte Carlo Program for the Simulation of X-Ray

    Emission in Electron Probe Microanalysis. *Microscopy and Microanalysis*, *23*(3), 634–646.

    https://doi.org/10.1017/S1431927617000526

Llovet, X., & Salvat, F. (2018). Influence of simulation parameters on the speed and accuracy of

    Monte Carlo calculations using PENEPMA. *IOP Conference Series: Materials Science and*

    Engineering, *304*(1), 012009. https://doi.org/10.1088/1757-899X/304/1/012009

Mahan, B., Siebert, J., Blanchard, I., Borensztajn, S., Badro, J., & Moynier, F. (2018b). Constraining

    compositional proxies for Earth's accretion and core formation through high pressure and high

    temperature Zn and S metal-silicate partitioning. *Geochimica et Cosmochimica Acta*, *235*, 21–

    40. https://doi.org/10.1016/j.gca.2018.04.032

Mahan, B., Siebert, J., Blanchard, I., Badro, J., Kubik, E., Sossi, P., & Moynier, F. (2018a).

    Investigating Earth's Formation History Through Copper & Sulfur Metal-Silicate Partitioning

    During Core-Mantle Differentiation. *Journal of Geophysical Research: Solid Earth*, 123, 8349-

    8363. https://doi.org/10.1029/2018JB015991

Pouchou, J. L. (1996). Use of Soft X-rays in Microanalysis. In Benoit D., Bresse, J.F., Van't dack L., Werner, H., Wernisch J. (eds.) *Microbeam and Nanobeam Analysis. Mikrochimica Acta Supplement* 13, Springer, Vienna, 39-60. https://doi.org/10.1007/978-3-7091-6555-3_3

Reed, S. J. B., & Long, J. V. P. (1963). Electron-Probe Measurements near Phase Boundaries. In H. H. Pattee, V. E. Cosslett, & A. Engström (Eds.), *X-ray Optics and X-ray Microanalysis* (pp. 317–327). Academic Press. https://doi.org/10.1016/B978-1-4832-3322-2.50035-4

Righter, K., Drake, M. J., & Yaxley, G. (1997). Prediction of siderophile element metal-silicate partition coefficients to 20 GPa and 2800°C: the effects of pressure, temperature, oxygen fugacity, and silicate and metallic melt compositions. *Physics of the Earth and Planetary Interiors*, *100*(1–4), 115–134. https://doi.org/10.1016/S0031-9201(96)03235-9

Rubie, D. C., Frost, D. J., Mann, U., Asahara, Y., Nimmo, F., Tsuno, K., et al. (2011). Heterogeneous accretion, composition and core–mantle differentiation of the Earth. *Earth and Planetary Science Letters*, *301*(1–2), 31–42. https://doi.org/10.1016/j.epsl.2010.11.030

Salvat, F. (2015). PENELOPE-2014: A code system for Monte Carlo simulation of electron and photon transport. In *Workshop Barcelona, Spain, 29 June – 3 July 2015*. *OECD/NEA Data Bank* (NEA/NSC/DOC(2015)3). Retrieved from https://www.oecd-nea.org/science/docs/2015/nsc-doc2015-3.pdf

Siebert, J., Corgne, A., & Ryerson, F. J. (2011). Systematics of metal–silicate partitioning for many siderophile elements applied to Earth's core formation. *Geochimica et Cosmochimica Acta*, *75*(6), 1451–1489. https://doi.org/10.1016/j.gca.2010.12.013

Siebert, J., Badro, J., Antonangeli, D., & Ryerson, F. J. (2012). Metal–silicate partitioning of Ni and Co in a deep magma ocean. *Earth and Planetary Science Letters*, *321–322*, 189–197. https://doi.org/10.1016/j.epsl.2012.01.013

Siebert, J., Badro, J., Antonangeli, D., & Ryerson, F. J. (2013). Terrestrial Accretion Under Oxidizing Conditions. *Science*, *339*(6124), 1194–1197. https://doi.org/10.1126/science.1227923

Siebert, J., Sossi, P. A., Blanchard, I., Mahan, B., Badro, J., & Moynier, F. (2018). Chondritic Mn/Na ratio and limited post-nebular volatile loss of the Earth. *Earth and Planetary Science Letters*, *485*, 130–139. https://doi.org/10.1016/j.epsl.2017.12.042

Suer, T.-A., Siebert, J., Remusat, L., Menguy, N., & Fiquet, G. (2017). A sulfur-poor terrestrial core inferred from metal–silicate partitioning experiments. *Earth and Planetary Science Letters*, *469*, 84–97. https://doi.org/10.1016/j.epsl.2017.04.016

Wade, J., & Wood, B. J. (2005). Core formation and the oxidation state of the Earth. *Earth and Planetary Science Letters*, *236*(1), 78–95. https://doi.org/10.1016/j.epsl.2005.05.017

Wade, J., & Wood, B. J. (2012). Metal–silicate partitioning experiments in the diamond anvil cell: A comment on potential analytical errors. *Physics of the Earth and Planetary Interiors*, *192–193*, 54–58. https://doi.org/10.1016/j.pepi.2011.12.002

Walter, M. J., Newsom, H. E., Ertel, W., & Holzheid, A. (2000). Siderophile Elements in the Earth and Moon: Metal/Silicate Partitioning and Implications for Core Formation. In *Origin of the Earth and Moon* (pp. 265–289). Tucson: University of Arizona Press. Retrieved from http://adsabs.harvard.edu/abs/2000orem.book..265W

Wood, B. J., Walter, M. J., & Wade, J. (2006). Accretion of the Earth and segregation of its core. *Nature*, *441*(7095), 825–833. https://doi.org/10.1038/nature04763
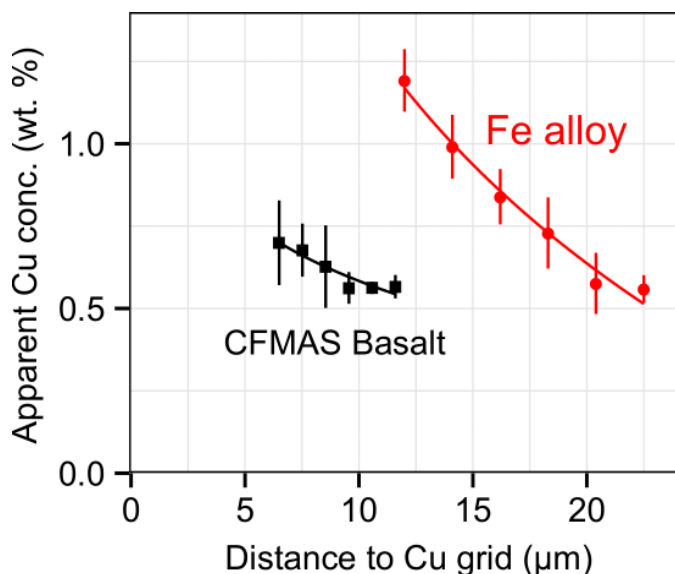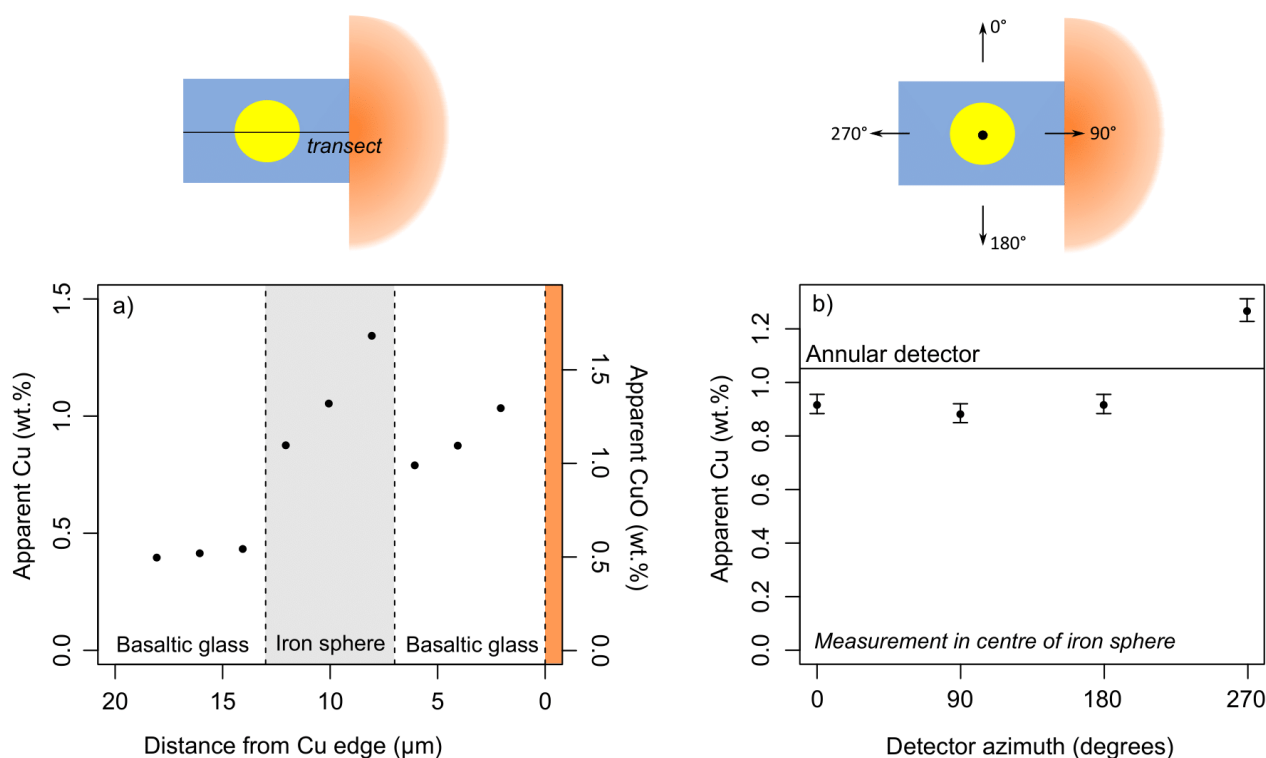
Figures

Figure 1 Apparent Cu concentration (wt.%) measured in Cu-free CFMAS basaltic glass (same composition as that simulated in this study) and Fe-rich alloy ($Fe_{17}WMoNi$) lamellae, both prepared by FIB and welded to a Cu TEM grid. EPMA measurements made at 15 keV with a 15 nA focused beam (for details see Jennings et al., 2019). Figure after Jennings et al. (2019); used with permission from Cambridge University Press.
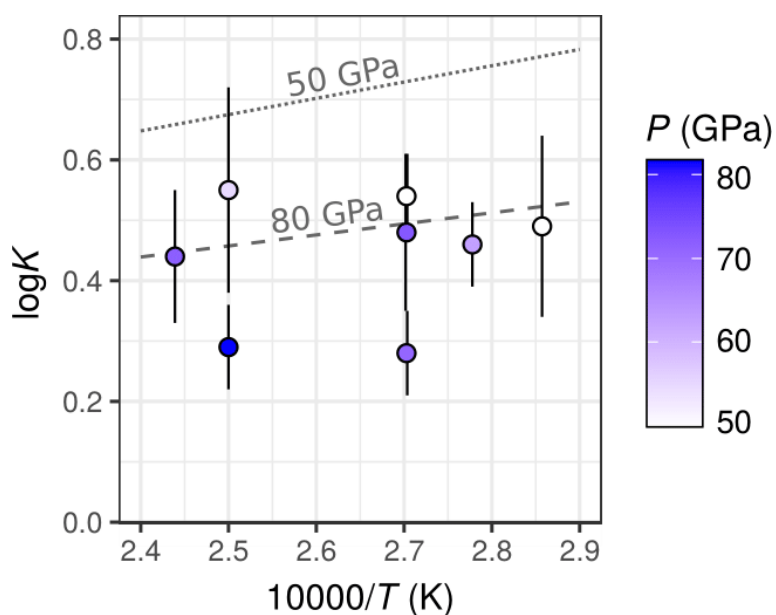

Figure 2 Cu partitioning data from the DAC experiments of Mahan et al. (2018a), presented as $\log K_{Cu}^{met\text{-}sil}$ as a function of 10000/T (K). K is an activity-corrected form of the mole fraction ratio

$(X_{Cu}^{metal}(X_{FeO}^{silicate})^{1/2})/(X_{CuO_{1/2}}^{silicate}(X_{Fe}^{metal})^{1/2})$. Error bars are 1σ. Also shown are the fitted PT-dependent

trends of Mahan et al. (2018a), who included low-P large-volume press data in the fitting dataset.

The high-P data, despite being included in the fit, match the model poorly and all data points are

almost within 1σ uncertainty of one-another.

Figure 3 Results of simulations. a) Apparent Cu and CuO concentration (wt.%) along a transect

through the Cu-free sample, measured using an annular detector. 2σ uncertainties are smaller

than the symbol size. Transect path is shown. b) The beam was directed on the metal ball centre

(black point), and the arrows show the directions to four detectors with 10° wide azimuthal opening

(centred at at 0°, 90°, 180° and 270°) relative to the sample position, that correspond to the plot

below. For comparison, the line in figure (b) shows the concentration measured using an annular

detector. Uncertainties are 2σ. All detectors in figures (a) and (b) have a latitudinal angular opening

of 10° centred on a 40° take-off angle.
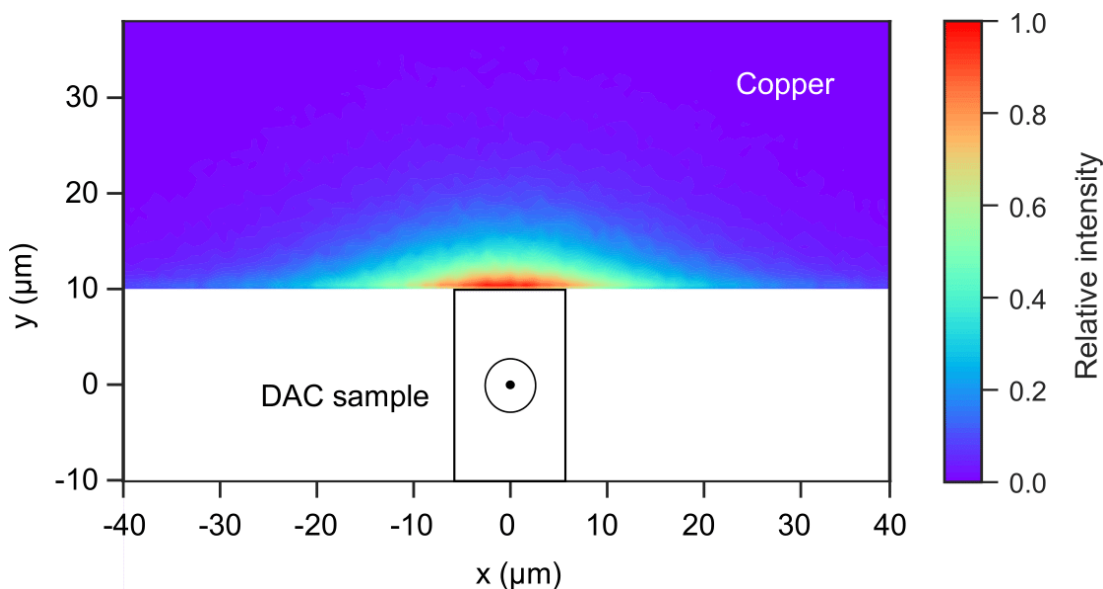
Figure 4 Generation of Cu-Kα_1 secondary X-rays mapped in x-y space (integrated through z). Scale in µm, beam is focused on (0,0) on the centre of the iron sphere, colour scale is linear and shows intensity of Cu Kα_1 secondary X-ray generation relative to the point with the maximum generated X-rays The copper block extends beyond the plot margins. Fluoresced X-rays can originate from rather far into the copper, with noticeable signal generated 10 µm away from the interface in the y direction.
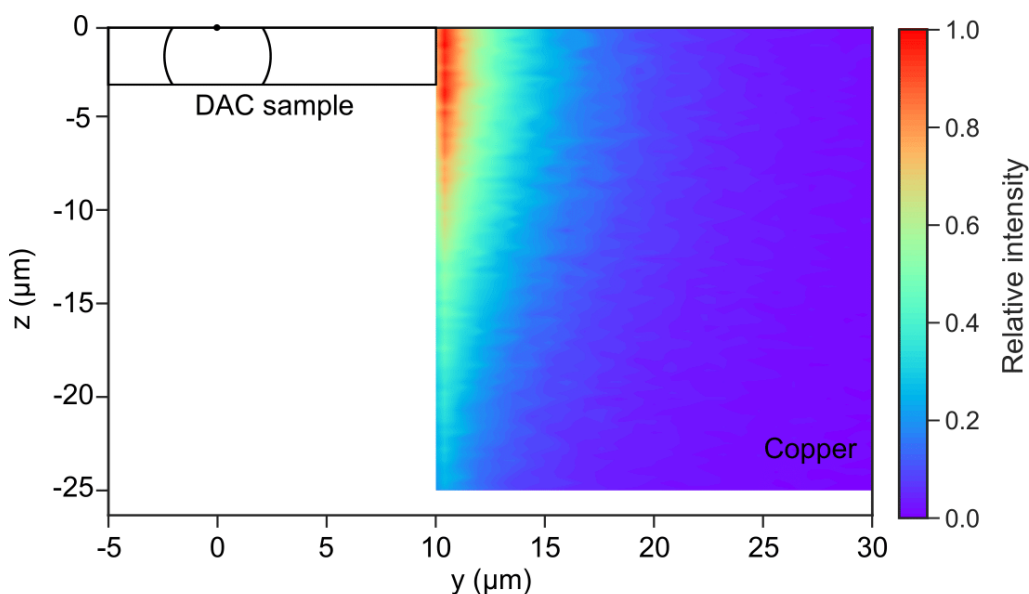
Figure 5 Generation of secondary Cu-Kα_1 X-rays mapped in y-z space (integrated through x). Colour scale as in Figure 4. The Cu block is 25 µm thick and extends off the plot in y. Secondary

fluoresced X-rays mostly originate from close to the face of the copper block onto which the sample is welded, through its full depth, such that a thicker Cu grid would be expected to yield a slightly higher secondary X-ray flux.
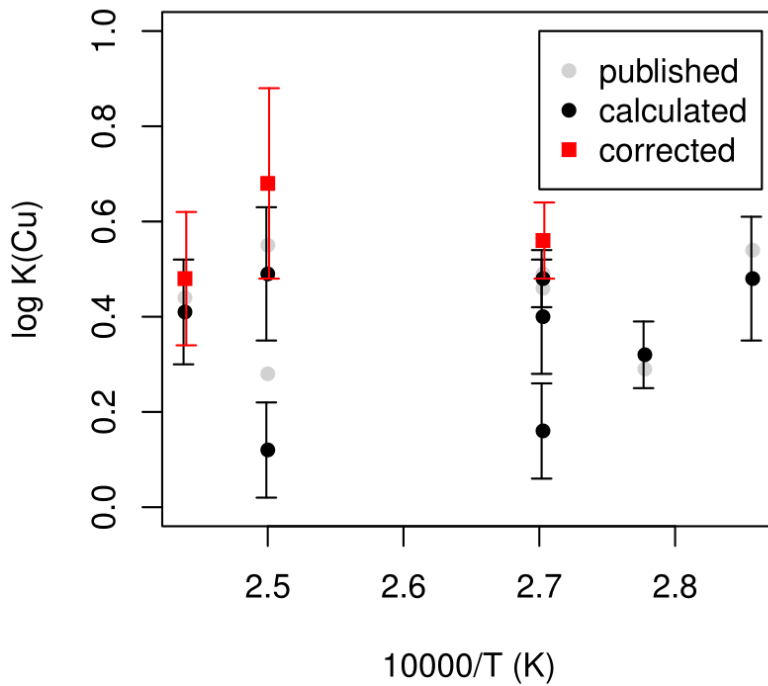
Figure 6 $\log K_{Cu}^{met\text{-}sil}$ of Mahan et al. (2018a) plotted as a function of $10000/T$. Pale grey circles are the published values; black circles are calculated by us; red squares are calculated following a linear correction for fluoresced Cu. Uncertainties are 1σ. We were unable to exactly reproduce published $\log K_{Cu}^{met\text{-}sil}$ values because some elemental concentrations are unreported.